Multifunctional Porous Asphalt Mixture Containing Metallic Blast Furnace Dust for Self-Healing Permeable Pavements

Andres Silva-Balaguera[a,b], Jose L. Concha[c], Manuel Chavez-Delgado[d], Luis A. Sañudo-Fontaneda[b], Richard Johnston[e], Jose Norambuena-Contreras[f,*]

[a]*GIISAG, Escuela de Ingeniería Civil, Universidad Pedagógica y Tecnológica de Colombia, Sede Tunja, 150001, Colombia*
[b]*Civil, Environmental and Geomatics Engineering Research Group (CEGE), Department of Construction and Manufacturing Engineering, University of Oviedo, Polytechnic School of Mieres, 33600 Mieres, Spain*
[c]*LabMAT, Departamento de Ingeniería Civil y Ambiental, Facultad de Ingeniería, Universidad del Bío-Bío, Concepción 4051381, Chile*
[d]*Departamento de Ingeniería Civil, Facultad de Ingeniería, Sede Concepción, Universidad Andres Bello, Chile*
[e]*Advanced Imaging of Materials (AIM) Core Facility, Faculty of Science and Engineering, Swansea University, SA1 8EN Swansea, United Kingdom*
[f]*Advanced Bituminous Materials Laboratory, Department of Civil Engineering, Faculty of Science and Engineering, Swansea University, SA1 8EN Swansea, United Kingdom*

**Corresponding author:* j.norambuena@swansea.ac.uk

Abstract

This paper evaluates the effect of adding Blast Furnace Dust (BFD), a by-product of the steel industry, on the multifunctional performance of porous asphalt mixtures designed for self-healing permeable pavements. Porous mixtures were prepared with six different BFD percentages (i.e., 0%, 2%, 4%, 6%, 8%, 10% by weight), as substitutes for fine aggregate. The physical, mechanical, hydraulic, electrical, thermal, and self-healing properties of the porous asphalt mixtures were subsequently evaluated. The effect of the chemical, mineralogical, and physical properties of both the aggregate and BFD on microwave heating and healing efficiency was also examined. The healing capability of the mixtures was quantified by measuring the three-point bending strength of specimens before and after microwave-induced healing. X-ray micro-computed tomography (micro-CT) was also employed on core samples to assess the distribution of BFD and the internal porosity. Results showed that the lower density of BFD reduced air void content when used as a fine aggregate replacement. At 4% BFD, hydraulic permeability approached that of the reference mixture, due to its good void distribution and connectivity, as evidenced by µCT reconstruction analysis. Electrical resistivity and thermal conductivity were unaffected by BFD incorporation. Mechanical properties and durability improved under both dry and wet conditions, while energy efficiency during microwave exposure also increased. The highest heating rates were observed in BFD and fine aggregate components. Healing indices generally decreased from the third cycle onward; however, the 4% BFD mixture maintained a high healing index for an additional cycle without adverse effects. In short, incorporating BFD into porous asphalt mixtures improves mechanical performance, durability, and microwave heating efficiency, while supporting multifunctional pavement design and promoting sustainability.

Keywords: Porous Asphalt; Permeability; Metallic Waste; Thermophysical Properties; Self-Healing

1. Introduction

Climate change has accelerated markedly over the past 150 years, with the global mean temperature in 2022 recorded as 1.1 °C above pre-industrial levels. This warming has substantially altered global precipitation patterns, heightening the risk of flooding and creating significant challenges for road infrastructure [1]. To address this challenge, porous asphalt mixtures (PAM) are extensively used as permeable pavement surfaces due to their capacity to improve road safety by enhancing surface drainage, ensuring efficient water flow, and reducing the burden on stormwater systems, thus reducing the risk of aquaplaning, even in adverse weather conditions [2].

Standardised hydraulic permeability values for PAM typically range from 5800×10^{-5} cm/s [3] to 7000×10^{-5} cm/s [4], making them effective in managing surface runoff and improving safety conditions. For instance, specimens with a 14 mm maximum aggregate size and 16% air void content (AVC) exhibit significantly higher permeability, exceeding 11000×10^{-5}cm/s. This superior performance is attributed to an average void size of 2.2 mm and enhanced connectivity and tortuosity within the mixture [5]. However, environmental conditions and traffic loads can lead to the premature deterioration of PAM, promoting the development of microcracks, reducing their mechanical strength and durability over time [6]. To address this issue, the bitumen in asphalt pavements, a complex molecular organic bituminous material, exhibits relatively strong surface wetting and diffusion capabilities, which impart an intrinsic self-healing behaviour. This enables the closure of microcracks and, consequently, the recovery of stiffness and strength over the pavement's service life [7–9].

To enhance the self-healing capability of bituminous materials, various extrinsic self-healing techniques have been developed. Among these, external microwave radiation heating can effectively raise PAM temperature, thereby promoting microcrack repair [10–13]. Microwave heating for self-healing asphalt relies on non-ionising electromagnetic radiation to induce volumetric heating within the material. This occurs through the oscillation, rotation, or vibration of molecules resulting from the interaction between microwaves and the material's constituents [14, 15]. Consequently, the efficiency of this self-healing technique is influenced by the chemical composition of the bituminous matrix, the pavement's internal structure, and the presence of additives responsive to microwave radiation. On one hand, the porous multi-cavity structure of PAM facilitates multiple microwave reflections, thereby amplifying the heating effect [16]. On the other hand, the addition of ferrous or metallic particles, which possess high thermal conductivity, can enhance both the mechanical properties and the microwave self-healing capacity of PAM by improving heat generation.

Recent studies have extensively investigated the effect of incorporating metallic particles into PAM. For instance, steel wool fibres significantly boost resistance to ravelling, tensile strength, and water sensitivity in PAM [10]. Similarly, NiZn ferrite, when used as a filler at a 5% addition, optimises the dynamic modulus and extends the fatigue life of PAM, providing uniform heating and achieving a fatigue life extension ratio of 1.05 after 120 seconds of microwave exposure at 300 W [13]. However, steel wool fibres exhibit a reduction in the self-healing index from 80% to 58% over five cycles, with optimal performance observed at a 6% addition and heating to 80 °C for 75 seconds at 1000 W [12]. Additionally, aluminium shavings at 800 W provide the best results for indirect tensile strength (ITS) healing, with a healing index of 35-75% [17]. These results highlight the potential of electrically responsive metallic additives to enhance the self-healing capacity of PAM under electromagnetic or microwave exposure, while simultaneously offering a sustainable pathway to valorise industrial by-products, such as steel industry waste, in high-performance pavement design.

In the steel industry, the production of pig iron generates between 7 and 45 kg of BFD per ton of pig iron [18, 19]. Furthermore, steel industry by-products, including steel slag (SS) and electric arc furnace (EAF) slag, not only pose environmental challenges but also offer opportunities for sustainable utilisation in self-healing asphalt mixtures [20–22]. SS has been employed as a replacement for coarse aggregates. In contrast, EAF slag has been investigated as a substitute for fine aggregates (<2 mm) in dense asphalt mixtures, aiming to enhance microwave heating and improve mechanical performance [21, 23]. For example, replacing 3% fine aggregates with EAF slag increased the microwave healing rate by 50%, while basic oxygen furnace slag showed strong microwave absorption at 0.6–2.36 mm [21, 23]. In mixture comparisons, open-graded friction course OGFC-13 with 80% steel slag achieved a healing index of 90% in cycle 1, declining to 61% by cycle 5, whereas asphalt concrete AC-13 with 60% steel slag started at 76% and decreased to 56% [24].

Previous studies indicate that open-graded friction course asphalt mixtures achieve enhanced microwave heating efficiency, as dense, interconnected macropores are transformed into smaller, discrete pores. The formation of additional micropores is driven by the capillary flow of bitumen, which partitions macro- and mesopores into finer pores [16, 24]. Although air voids in open-graded friction course asphalt mixtures initially reduced resistance to moisture damage after two freeze-thaw cycles, microwave heating enhanced resilience, enabling up to five cycles. Freeze-thaw enlarges and connects pores, whereas microwave heating closes cracks and subdivides larger pores [24]. In summary, incorporating steel industry by-products such as BFD into PAM valorises industrial waste and promotes circular economy policies, improves self-healing performance, and promotes sustainable pavement design, reducing maintenance costs and dependence on virgin materials. However, key questions remain concerning its influence on the physical, hydraulic, mechanical, and electrical properties of PAM, as well as the effects of BFD on heating and healing under controlled microwave radiation.

The scope of this study focuses on the design of multifunctional porous asphalt pavements incorporating steel industry by-products, with hydraulic and self-healing properties activated through external microwave heating. This study specifically aims to: (i) assess the impact of varying BFD contents on the physical, hydraulic, mechanical, electrical, and thermophysical properties of PAM; (ii) examine the chemical and mineralogical factors controlling microwave absorption and heat generation in PAM and its components; and (iii) evaluate the effectiveness and durability of microwave-induced crack healing over multiple cycles. This integrated approach provides a comprehensive framework for the design of durable, hydraulically efficient, and self-healing permeable pavements, consistent with SUDS and circular-economy principles.

2. Materials and Methods

PAM samples containing varying proportions of BFD were systematically assessed for their physical, hydraulic, mechanical, electrical, and thermophysical properties. Figure 1 summarises the experimental workflow, illustrating the relationship between the materials and the experimental methods applied to the porous asphalt mixtures.

2.1. Raw materials

PAM were prepared in accordance with the Spanish PA-16 standard, employing polymer-modified bitumen PG 76-22. The aggregates were classified into three fractions: coarse aggregate or gravel, fine aggregate or sand, and filler. A bitumen content of 5 wt.% was adopted following preliminary laboratory tests, which showed that this proportion provided the best compromise between the physical, hydraulic, and mechanical characteristics of the PAM. BFD was used to partially replace the fine aggregate fraction to enhance the microwave heating capacity of the mixtures (see Figure 1). The particle size distribution (see Figure 2) remained constant across mixtures, with fine aggregates replaced in the 0.075 – 2 mm range. A detailed characterisation of the bitumen, coarse and fine aggregates with and without BFD replacement is given in **Tables S1, S2 and S3 of the supplementary material**, respectively.

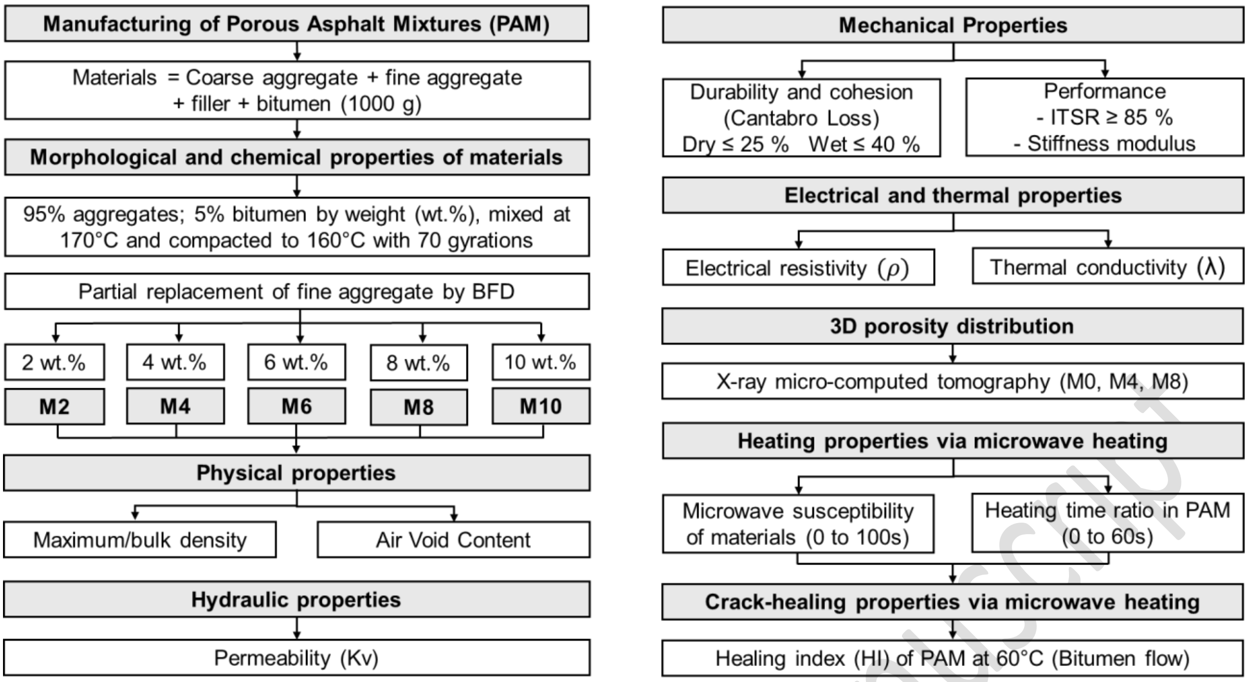

Figure 1. Flowchart detailing the materials and experimental methods for the PAM.

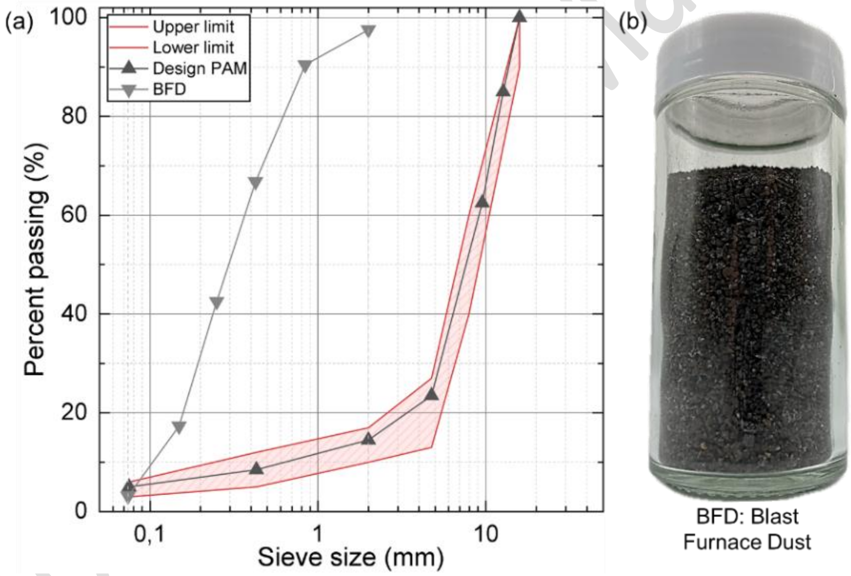

Figure 2. (a) Granulometry distribution of aggregates and BFD used for asphalt mixture manufacturing, and (b) example of BFD ranged between 2 mm and 0.074 mm sieve size.

2.2. Morphological and chemical properties of raw materials

The optical properties of the minerals within the aggregates were analysed in thin sections using a Meiji MT9000 optical microscope (Petrographic), as shown in Figure 3(a–c). The morphology of the aggregates and BFD was evaluated through Scanning Electron Microscopy (SEM) using a ZEISS EVO MA10. Figure 3(d) and (e) shows representative SEM images of the ground aggregate, characterised by a rough surface which improves adhesion with the bitumen. Regarding the characterisation of the BFD depicted in Figure 3(f), SEM images were recorded, identifying a rough and porous surface (see Figure 3 (g) and (h)) with pore sizes between 10-30 µm, improving the cohesion of the mixtures. The chemical composition of the aggregates and BFD was obtained through X-ray fluorescence (XRF) tests (see Table 1). Finally, the mineral composition of the aggregates and BFD was determined by X-ray diffraction (XRD), with results provided in Table 2 and Table 3, respectively.

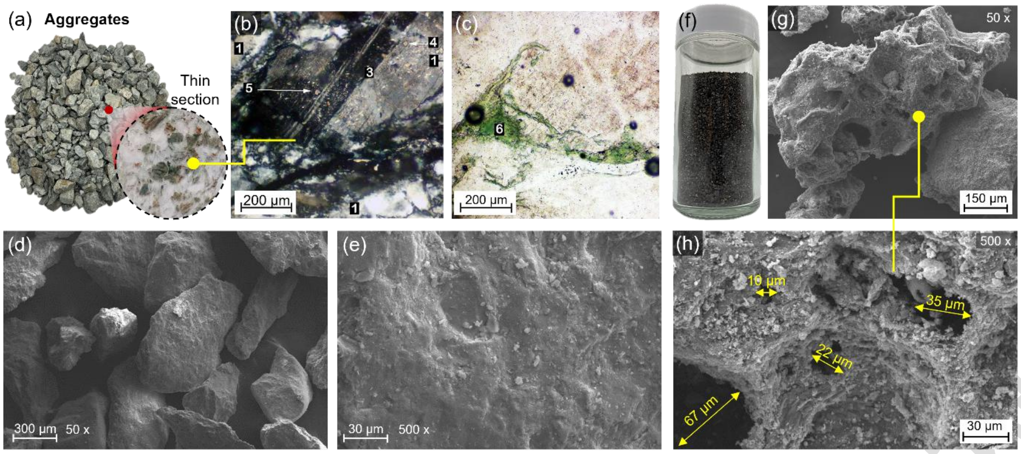

Figure 3. Detail of (a) aggregates showing (b) recrystallised quartz crystals with crenulated edges (1), relicts of plagioclase porphyroclasts (3), calcite (4), sericite (5), and (c) chlorite (6); representative SEM images showing (d) ground aggregates and their (e) surfaces; (f) BFD particles and SEM images of their (g) surfaces and (h) porosity.

Table 1. Chemical elements (XRF) present in aggregates and BFD.

Element	Si	Al	Fe	Ca	K	Ti	Mn	S	Zn
Aggregates concentration (%)	46.7	18	15.5	13	5.2	1.2	0.3	0.3	-
BFD concentration (%)	2.2	5.8	75.6	7.8	0.6	-	2.6	1.8	3.1

Table 2. Mineral composition (XRD and petrographic) of the aggregates (Mylonite).

Mineral	Quartz	Orthoclase*	Microcline*	Chlorite	Plagioclase*	Hornblende	Sericite*	Calcite
Chemical compound	SiO_2	$KAlSi_3O_8$	$KAlSi_3O_8$	$Fe_3Si_4O_{10}(OH)_2$	$NaAlSi_3O_8$	$Ca_2Fe_5Si_8O_{22}(OH)_2$	$KAl_2(AlSi_3O_{10})(OH)_2$	$CaCO_3$
Weight (%)	34	32	10	8	5	5	2	2

Note: *Feldspar minerals.

Table 3. Mineral composition (XRD) of the Blast Furnace Dust (BFD).

Mineral	Magnetite	Hematite	Siderite	Wüstite	Quartz	Calcite	Lime	Sillimanite	Groutite
Chemical compound	Fe_3O_4	Fe_2O_3	$FeCO_3$	FeO	SiO_2	$CaCO_3$	CaO	Al_2SiO_5	MnO_2
Weight (%)	29.2	15.4	15.3	11.8	15.6	5.3	3.0	2.8	1.7

2.3. Manufacturing of the PAM test specimens

PAM test specimens were manufactured according to the method described in **Figure S1 of the supplementary material**. Firstly, the aggregates and BFD were heated to 170 °C for 24 h, while the bitumen was conditioned at 170 °C for 2 h before mixing. Then, the raw materials were mixed in a metallic bowl in the following order: (1) coarse aggregate, (2) fine aggregate (with and without BFD replacement), (3) bitumen, and (4) filler. As for the specimens including BFD, the additive was added at six percentages as a weight replacement for fine aggregate: 0%, 2%, 4%, 6%, 8%, and 10 wt.%. These values were selected based on preliminary tests, which demonstrated that BFD contents of ≤10% produce detectable changes in properties without adversely affecting the manufacture of the mixtures. The raw materials were mixed for 5 min at 170°C. Once the aggregates were fully coated with bitumen, the mixture was poured into a pre-heated Superpave Gyratory Compactor mould and compacted with 70 gyrations at 160 °C. The compaction criterion was defined to achieve an air void content close to 20% in M0. Then, the samples were extracted from the mould and conditioned to room temperature (~20 °C) for 24 h once compacted. In addition, different test samples were prepared to characterise the physical, electrical, thermal, and self-healing properties of each mixture as follows:

- *Superpave specimens:* Specimens with dimensions of 100 mm diameter and 62 ± 1 mm height. They were used for the measurement of bulk specific gravity, hydraulic permeability, particle loss resistance, indirect tensile strength, and indirect tensile stiffness modulus.
- *Cylindrical samples:* Three Superpave specimens per mixture type were selected and cut on each external face, producing samples with a height of 50 mm and a diameter of 100 mm. These were used to measure electrical resistivity and thermal conductivity. Three cylindrical samples (50 mm diameter × 50 mm height) were also used for X-ray micro-computed tomography tests on mixtures containing 0%, 4%, and 8% BFD.
- *Semicircular samples:* The modified Superpave samples were cut through two opposite planes, producing quarter samples with approximate dimensions of 100 mm length, 50 mm height, and 25 mm width. A notch 5 mm thick and 10 mm deep was introduced at the midpoint along the loading direction. These samples were used for microwave heating and self-healing measurements.

Finally, each test specimen was labelled with an MX code, where "M" denotes the mixture and "X" indicates the BFD replacement content (0%, 2%, 4%, 6%, 8%, 10 wt.%). For example, M10 corresponds to a mixture with 10% by weight BFD replacing fine aggregates.

2.4. Physical properties of PAM test specimens

The bulk specific gravity (Gsb) was determined following ASTM D1188M [25]. Dry mass and the real volume of the Superpave specimens were determined from water-submerged test specimens at 20 °C. The maximum specific gravity (Gsm) of the mixtures was measured according to the ASTM D2041 [25], using loose asphalt samples submerged in deionised water at 20 °C in continuous agitation. A vacuum of 4 kPa was applied for 15 minutes, with continuous vibration to ensure full saturation. Finally, with the calculus Gsm and Gsb, the Air Void Content (AVC) was calculated in accordance with ASTM D3203M [25], and the representative AVC content for each PAM sample was determined as the average of twenty measurements.

2.5. Hydraulic permeability of PAM specimens

The hydraulic permeability was determined based on the Florida Method [26], using a falling head infiltrometer (see setup in Figure 4). The method consisted of measuring the time required for 500 mL to pass through the test specimen, and a correct reading was considered when the difference between the first and third tests was ±4.0 %. The permeability coefficient (kv) was determined based on Darcy's Law equation, being determined as the mean of three measurements.

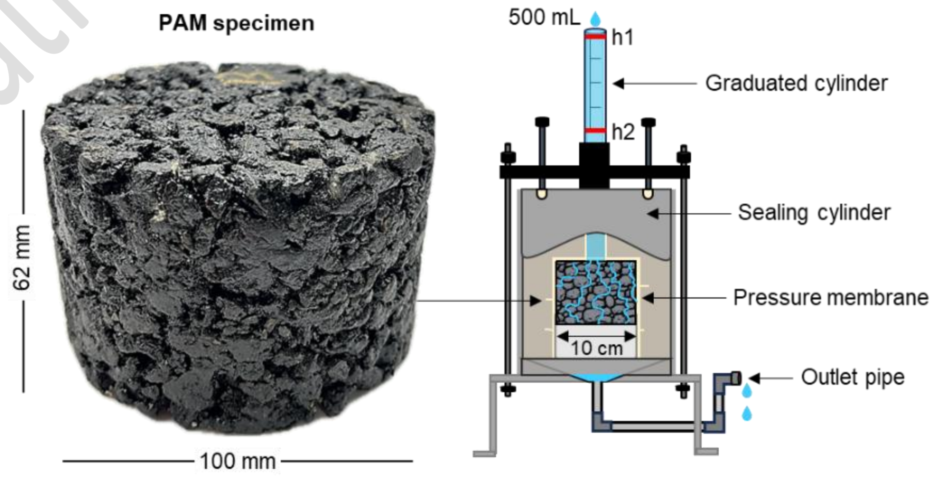

Figure 4. Hydraulic permeability test of PAM specimens.

2.6. Mechanical properties of the PAM specimens

The effect of the BFD additive on the particle loss and disintegration resistance of the PAMs under dry and wet conditions was evaluated by the Cantabro test (particle loss) [27, 28] in accordance with NLT-352/86 standard [27]. Additionally, the ITS test was performed on the PAM samples under dry and wet conditions according to ASTM 7064-13 [29]. The Tensile Strength Ratio (TSR) was calculated from this method as the proportion of the ITS values between dry and wet samples with similar void and permeability conditions. The stiffness of the PAM specimens was measured by a tensile strength test, in accordance with the European Standard UNE EN-12697-26:2019 Annexe C [30]. Finally, the representative values of particle loss, ITS, and stiffness were determined as the average of five measurements.

2.7. Electrical and thermal conductivity of PAM specimens

The susceptibility of PAM samples to electrical conductivity as a result of BFD content was evaluated using an electrical resistivity test, based on Ohm's second law and the method described in Norambuena-Contreras et al. [31]. For this, the electrical resistance of PAM samples was measured using a 500 V megohmmeter (Hioki, model IR 4056) connected to two 10×15 cm stainless steel electrode plates. A pressure of ≈1 kPa was applied to ensure good contact and stable, noise-free electrical resistance measurements. In addition, the thermal conductivity of PAM samples was measured using the thermal needle probe method, as described in Norambuena-Contreras et al. [31]. A KD2-Prothermal Properties Analyser (Decagon Devices Inc.) was equipped with a handheld controller and the RK-1 needle-shaped sensor. The sensor was coated with a thermal compound to minimise air gaps and inserted into pre-drilled PAM samples. Each sample containing BFD was stacked on two identical BFD samples for consistent heat transfer. Electrical resistivity and thermal conductivity for each test sample were then determined as the mean of three measurements.

2.8. X-ray micro-computed tomography of PAM samples

X-ray microtomography (μCT) scans of the M0, M4, and M8 samples were performed using a Nikon XT H225 microfocus system equipped with a 1.3 MP Varian PaxScan 2520 flat-panel detector in reflection mode with a tungsten target. All scans were conducted under identical conditions: 145 kV tube voltage, 75 μA current, 1420 ms exposure, and 3015 projections, yielding a voxel size of 39.86 μm. A 0.5 mm tin (Sn) filter was placed between the source and the sample to refine the X-ray beam. Tomograms were reconstructed using CTPro 3.0 (Nikon Metrology) with a cone-beam filtered back-projection algorithm. Reconstructed data were processed in Dragonfly World 2024.1 (Comet Technologies, Canada) to generate 2D grayscale slices and 3D volumes. Porosity was segmented, visualised, and quantified, while the thickness meshing module was used to calculate 3D porosity thickness and determine percentage AVC area profiles as a function of depth.

2.9. Microwave heating of PAM and its individual components

The heating efficiency of the PAM and its components (i.e., coarse aggregate, fine aggregate, BFD, filler, and bitumen) was evaluated under microwave radiation, following the procedure defined by Norambuena-Contreras et al. [32] (see setup in Figure 5). Microwave heating was evaluated for the raw materials in PAM, according to their proportional weight in the mixture design, following the three steps provided below:

- *Step 1:* The natural aggregates and BFD were washed, dried above 100 °C, and conditioned at 20 °C in a controlled chamber.

- *Step 2*: Each raw material sample was placed in a marked ceramic container to ensure consistent positioning and was heated in a microwave oven (700 W, 2.45 GHz) for 100 seconds at 10-second intervals.
- *Step 3*: The surface temperature of each sample was recorded using a thermal camera (*HIKMICRO, model M30*) with a resolution of 384×288 pixels, a measurement range of −20 to 170°C, and a precision of ±2%.

Then, using the same microwave equipment, PAM semi-circular samples were heated for 60 seconds at 10-second intervals, see Figure 5(c). During this period, energy consumption was measured using a High-Power Monitor GM89, operating at 220 V and 50 Hz. Finally, the representative temperature distribution of each raw material and PAM sample was determined as the mean of three measurements.

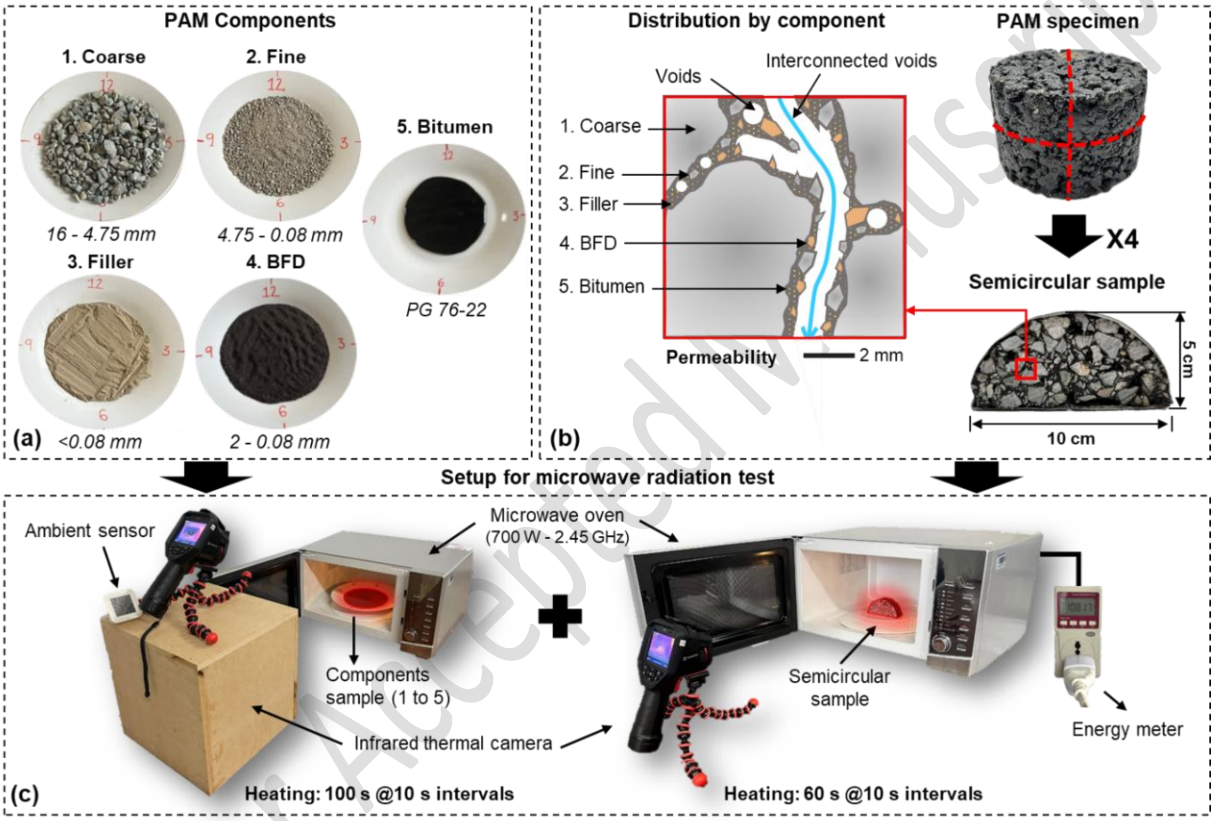

Figure 5. Representation of (a) PAM components, (b) a semicircular PAM sample heated under microwave radiation, and (c) evaluation of the superficial heating of both test samples under microwave radiation.

2.10. Crack-healing capacity of PAM via microwave heating

The microwave crack-healing test for PAMs was conducted on semi-circular samples using a four-step cyclic method: (i) conditioning, (ii) fracture, (iii) heating, and (iv) healing, as described by Norambuena-Contreras et al. [31] and summarised as follows, see Figure 6:

- *Step 1. Conditioning*: The test samples were pre-conditioned for 2 h at 5°C.
- *Step 2. Fracture*: The samples were fractured using a three-point semicircular bending test at a speed of 0.5 mm/min. Then, the samples were conditioned at room temperature for 4 h.
- *Step 3. Microwave heating*: The fractured samples were carefully realigned and exposed to microwave heating for an optimal healing time using a microwave oven.
- *Step 4. Healing*: Afterwards, the samples were left at room temperature for 12 h at 20°C, repeating step 1 and completing one cycle.

The healing index (HI) was determined as the ratio of the maximum force recorded during the fracture process, before ($F_{initial}$) and after (F_{healed}) the healing process. Finally, each PAM test sample underwent five crack-healing cycles to evaluate the efficacy of the healing methodology at different stages of the asphalt mixtures. The representative HI value for each PAM healing cycle was calculated as the mean of eight measurements.

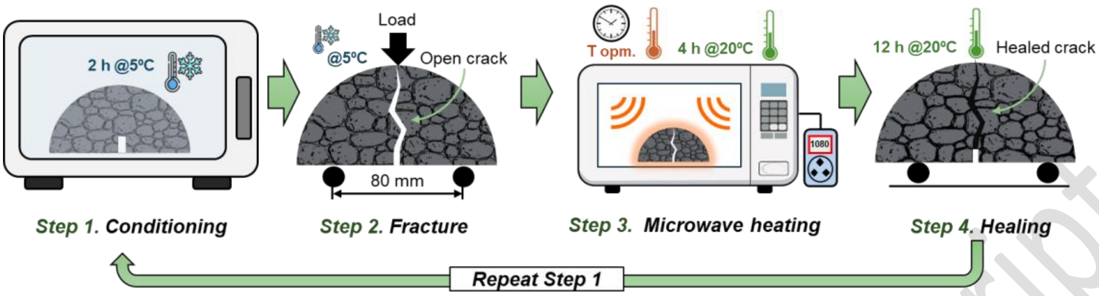

Figure 6. Schematic representation of crack-healing cycle using microwave heating.

3. Results and Discussions

3.1. Effect of the addition of BFD on the physical and hydraulic properties of PAM

Figure 7(a) presents the average results for the maximum density and bulk density of the mixtures. Overall, the evaluated mixture designs show a decrease in maximum density from 2.48 g/cm³ for M0 to 2.42 g/cm³ for M10, while the bulk density of all mixtures remained nearly constant at approximately 2.00 g/cm³. This effect can be attributed to the low density and inherent internal porosity of BFD, which, relative to its weight, occupies a larger volume in the mixture, thereby reducing the maximum density. Additionally, as the proportion of BFD increases, the AVC of the mixtures decreases due to the reduction in maximum density, as shown in Figure 7(b). Incorporation of BFD slightly reduced the AVC from 19.2% (M0) to 17.6% (M10).

Furthermore, the volumetric relationships in asphalt mixtures were analysed using a phase diagram (**Figure S2**), considering parameters such as AVC, effective bitumen, absorbed bitumen, and voids filled with bitumen. With the addition of BFD, the angularity and absorption of the fine fraction (**Table S3**) increased. The increase of BFD raises the effective bitumen content, suggesting enhanced performance in mixtures M2 to M6. Conversely, low bitumen absorption observed in the aggregates of M8 and M10 is attributed to high bitumen absorption of BFD, which may potentially compromise the strength and durability of the asphalt pavement structure. This hypothesis is evaluated through the mechanical analysis presented in Section 3.2.

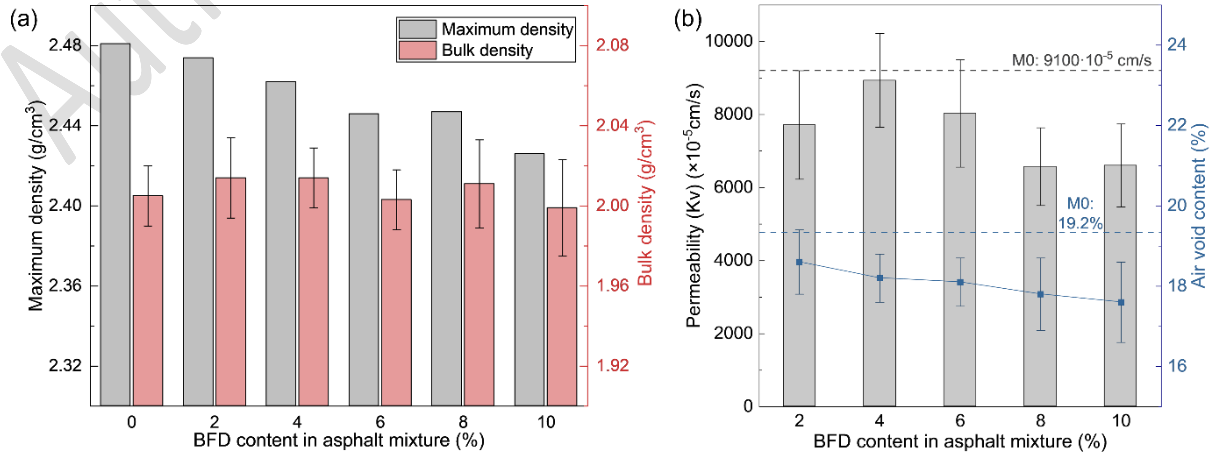

Figure 7. (a) Results of maximum density and bulk density, (b) permeability and air voids content in the asphalt mixtures with different BFD content.

Regarding the hydraulic permeability property, Figure 7(b) also shows that the average hydraulic permeability was decreased with the increment of the BFD content from 7700×10^{-5} cm/s for the M2 to 6600×10^{-5} cm/s in M10. This result is primarily attributed to the reduction of AVC in the mixtures [33]. The notably similar permeability values for the M8 and M10 samples, approximately 6600×10^{-5} cm/s, can be explained by their low AVC (17.6%). Additionally, M4 exhibited an average permeability value closer to that of M0. The similarity in permeability for M4 can be attributed to the comparable average AVC contents of 19.2% for M0 and 18.1% for M4, as well as to the tortuosity of the mixtures. Variations in tortuosity and BFD composition were examined using the μCT scan of a cored sample from each porous asphalt mixture (see Figure 8(a–c)) and analysed in terms of raw material and porosity distribution. From the top view, M0 exhibited fewer but larger voids than M4 and M8, the latter having smaller and more isolated voids. Complementarily, the frontal and 3D views reveal that M0 and M4 share similar void sizes and distributions. For these results, it can be concluded that M0 and M4 possess more interconnected voids compared to M8, see Figure 8(b).

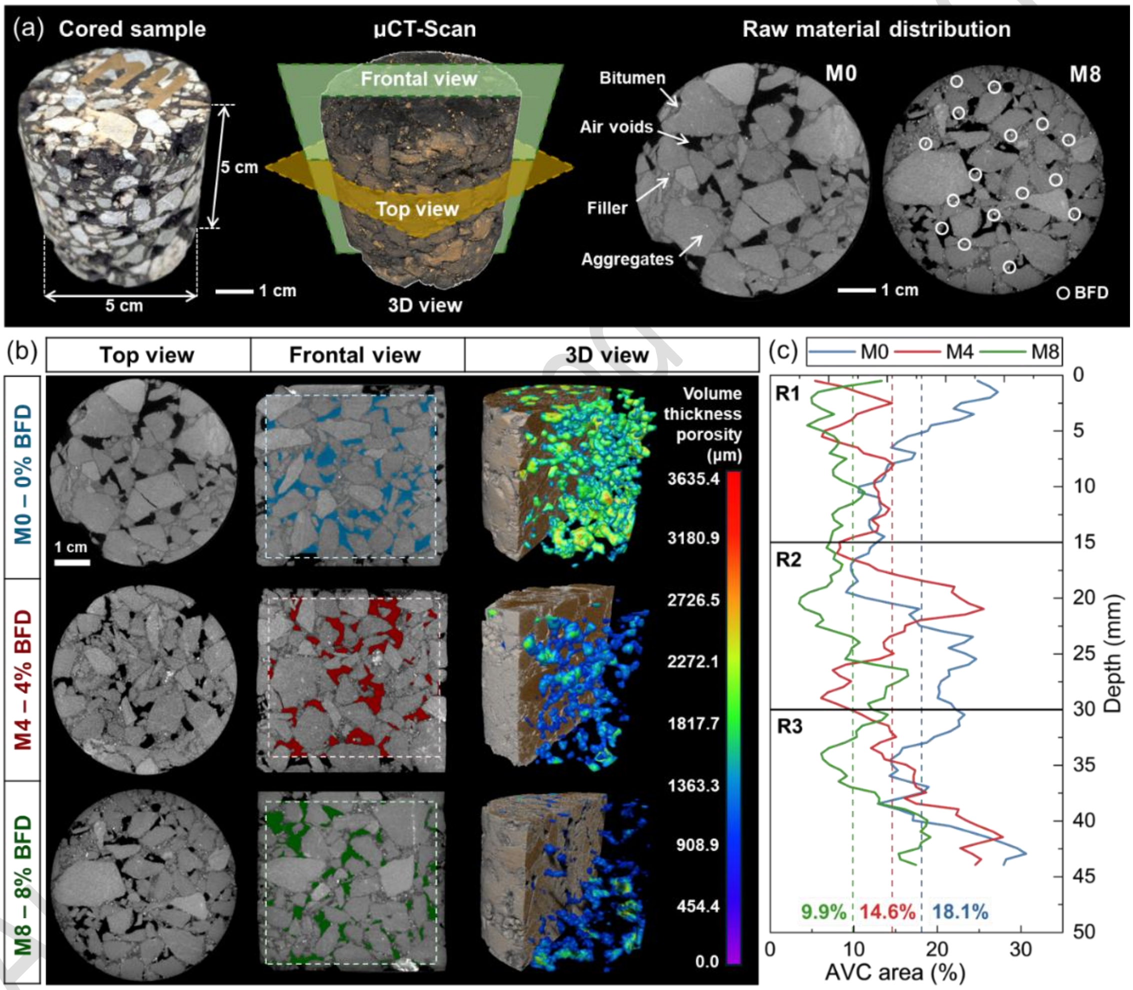

Figure 8. (a) Cored sample and μCT scan showing the raw material. (b) Top, frontal, and 3D μCT images of cored samples. (c) Percentage AVC area profile with depth for M0, M4, and M8 divided by regions (R1-R3).

In addition, Figure 8(c) shows the percentage AVC area profile with depth for each mixture, quantified from μCT image analysis. A reduction in the total AVC is observed with the addition of BFD, decreasing from 18.1% (M0, blue line) to 9.9% (M8, green line), which is notably greater than the 1.6% reduction estimated from bulk density. This suggests a higher concentration of air voids near the sample boundaries, contributing to an overall increase in void content. Figure 8(c) also presents the μCT-derived spatial distribution profile of AVC for the cored samples, divided into three depth regions: R1 (0–15 mm), R2 (15–30 mm), and R3 (30–45 mm). In samples M0, the AVC peak (≈22%) was evenly distributed, whereas M4 exhibited peaks of around 20% in regions R2 and R3. In the same regions, M8 showed peaks near 14%, indicating better compaction. The pronounced peaks in M0 and M4 suggest greater void connectivity and higher permeability. In contrast, M8 had lower AVC in R2, with a slight increase in R3, resulting in reduced permeability (see Kv results in Figure 7(b)). These results indicate that the effective bitumen content and BFD proportion in M4 (see 3D µCT reconstruction of M4 in **Video S1**) created pathways that promote water movement comparable to M0.

3.2. Effect of BFD addition on the mechanical properties of PAM

Figure 9 presents the average resistance to particle loss in dry and wet conditions, measured along with the Water Damage Factor (WDF). The average dry particle loss for M0 was 20.8%, while M2, M4, M6 and M8 recorded losses of 16.7%, 17.6%, 18.4% and 19%, respectively. Mixtures containing BFD showed improved resistance to particle loss compared with the reference mix, likely due to enhanced cohesion of the fine fraction and reduced voids. However, M10 exhibited a high particle loss (32%, AVC 17.6%), indicating that the additional fines increase bitumen absorption, thereby reducing the effective binder film thickness. This weakens the aggregate skeleton and inter-particle contact, promoting mixture disintegration rather than merely decreasing inter-particle friction. During the wet-state test at 60°C, water penetrates the bitumen–aggregate interface due to its lower density, reducing particle loss resistance as the small contact angle facilitates water ingress and weakens adhesion [34]. Mixtures containing 4–10% BFD exhibited markedly improved resistance compared with the reference mixes M0 and M2 (Figure 9). The average wet particle loss was 39.4% for M0 and M2, compared with 24.6%, 33.4%, 25.1%, and 34.6% for M4, M6, M8, and M10, respectively. Increasing the BFD content improves resistance to water-induced particle loss, as shown by the decrease in WDF from 2.3 for M0 to 1.1 for M10. This reduction indicates enhanced cohesion between the coarse aggregates and the asphalt mortar, attributed to the angularity and porosity of BFD, which strengthens bitumen adhesion. In short, incorporating 2–8% BFD in porous asphalt improves particle loss resistance under dry and wet traffic.

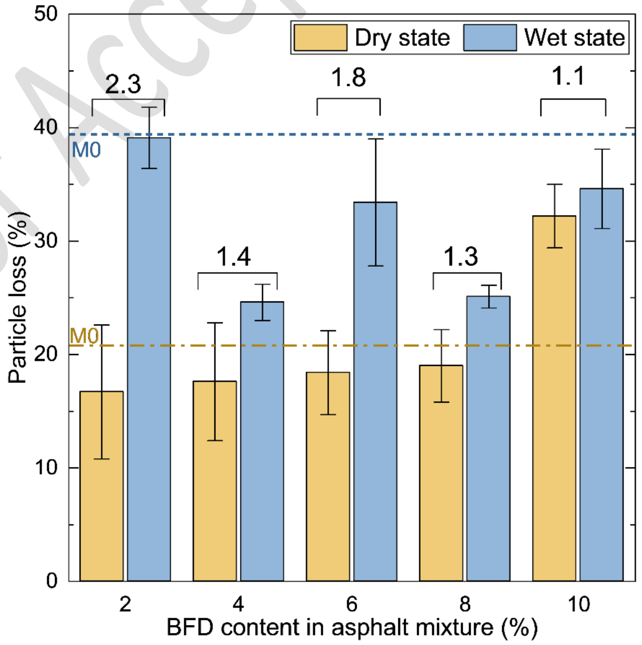

Figure 9. Results of particle loss in the asphalt mixtures with different BFD content.

Furthermore, Figure 10(a) presents a bar chart showing the mean values and error bars (±σ) of ITS in dry and wet conditions, as well as the ratio (ITSR) between the two in the mixtures. Under dry conditions, ITS values increase from 485 kPa for M0 to 531 kPa for M10, reflecting the influence of BFD content and reduced voids.

The rough, angular BFD particles and lower void content enhance the internal skeleton, strengthening mechanical interlocking. Under wet conditions, ITS rises slightly with BFD addition, from 445 kPa for M0 to 451 kPa for M6, reaching 475 kPa and 470 kPa for M8 and M10, respectively.

Correspondingly, ITSR decreases from 90% to 84% as BFD content increases from 2% to 6%, while 8% BFD achieves the highest ITSR of 94%, exceeding M0's 92% despite a slight reduction in dry strength. These results, consistent with particle loss tests, indicate that BFD addition maintains or reduces water sensitivity while improving mixture cohesion. Alternatively, increasing BFD content is associated with higher bitumen absorption, which reduces the effective bitumen content and weakens adhesion between the mortar and coarse aggregates [10, 24]. Supporting this observation, visual comparison of the failure surfaces of M0 (Figure 10(b)) and M10 (Figure 10(c)) revealed a substantial increase in coarse aggregates without bitumen in M10, contributing to its failure.

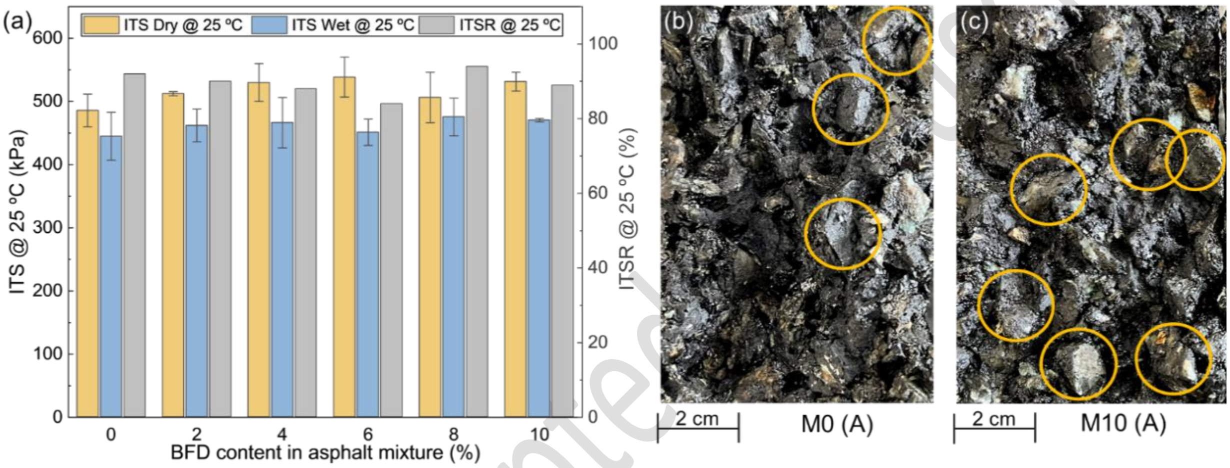

Figure 10. (a) Results of ITS and ITSR measured in the asphalt mixtures with different BFD content. Images of failure surfaces A in samples (b) M0 and (c) M10, showing cohesion loss in the asphalt aggregate.

Moreover, Figure 11(a) presents the average stiffness modulus of the mixtures, both with and without BFD, across different temperatures. It can be observed that the stiffness modulus of porous asphalt decreases with increasing test temperature, primarily due to bitumen's viscoelastic behaviour, which loses stiffness at higher temperatures.

Additionally, Figure 11(a) shows that incorporating BFD slightly increases the stiffness modulus of asphalt mixtures compared with those without BFD, irrespective of the testing temperature. Particularly, at low (5°C) and intermediate (25°C) temperatures, M4 exhibited higher average stiffness modulus than M0, with values of 5210 MPa and 507 MPa, respectively. This slight increase is attributed to reduced voids and improved mortar cohesion due to BFD distribution. At 25°C and 40°C, M10 showed a marked increase in modulus, with averages of 829 MPa and 158 MPa, corresponding to rigidity gains of +397 MPa and +68 MPa compared with M0. The overall increase in rigidity for M10 can be attributed to several factors: (i) the reduction in AVC, (ii) the lower bitumen content, and (iii) the resulting increase in aggregate-to-aggregate contact, as shown in Figure 10(c), which promotes interlocking of the aggregate particles.

Figure 11(b) also shows a direct relationship between stiffness modulus values measured in the longitudinal (A–A′) and transverse (B–B′) directions of the asphalt specimens, independent of BFD content and test temperature. These results indicate that porous asphalt modified with BFD does not exhibit significant anisotropic mechanical behaviour perpendicular to the coaxial axis, confirming uniform BFD distribution and consistent stiffness modulus across specimens. Consequently, BFD modification slightly enhances stiffness modulus, reduces aggregate loss (a common cause of premature ravelling), and may help mitigate this issue in asphalt mixtures [10].

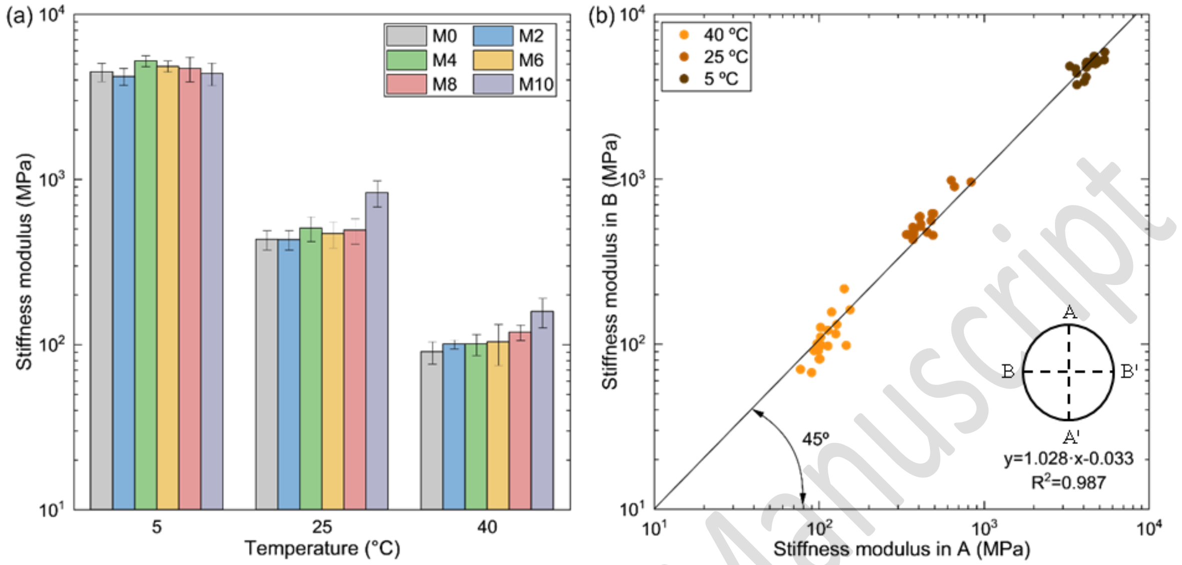

Figure 11. (a) Results of stiffness modulus in porous asphalt mixtures with and without BFD addition at different temperatures. (b) Correlation between stiffness modulus of test samples in longitudinal (A) and transverse (B) orientations.

Previous results demonstrate that adding BFD to porous mixtures improves mechanical performance by 2–8%, with 4% identified as the optimal content. The M4 mix shows enhanced aggregate–bitumen coating, cohesion, and flexibility, primarily due to bitumen absorption and adhesion to BFD. This improvement is attributed to the low density, high surface roughness, and porosity of BFD, which increase the contact area with bitumen, creating additional sites for mechanical bonding and chemical affinity [35]. A strong chemical affinity between aggregates and bitumen is essential for durable bonding (see Tables 1-3). Acidic minerals like quartz and plagioclase adhere well, while alkaline minerals enhance bonding with weakly acidic bitumen in dry conditions [36–39]. BFD's metal oxides and high CaO/(SiO2+P2O5) ratio (0.19 vs. 0.06 in aggregates) improve adhesion, supporting an optimal 4% replacement that enhances resistance without affecting voids. Although moisture can weaken bonds, carboxylic acids in bitumen bond effectively with BFD oxides and siliceous surfaces, reducing moisture damage (see results in Figure 9 and Figure 10). Fully coated coarse aggregates further minimise stripping. Porous asphalt mixtures with 4–6% BFD show improved mechanical performance under both dry and wet conditions, demonstrating the material's effectiveness in enhancing adhesion and durability.

3.3. Effect of the BFD addition on the electrical and thermal properties of PAM

Figure 12(a) displays a bar chart with the mean values and error bars (±σ) for the electrical resistivity measured for the mixtures, comparing different BFD contents with the reference sample. The reference mixture exhibits an average electrical resistivity of 2.6×10^7 Ω·m, while mixtures containing 2%, 4%, 6%, 8%, and 10% BFD show increased resistivities of 4.8×10^7, 6.9×10^7, 1.21×10^8, 8.6×10^7, and 5.1×10^7 Ω·m, respectively. The minimal variation between BFD-containing mixtures and the reference mixture indicates that the mixtures were not electrically conductive, corresponding to an insulating phase [40]. These results may be explained by the distribution of BFD within the mixtures (see CT results in Figure 8(a)), which forms groups that behave as isolated particles, inhibiting the development of conductive pathways within the porous mixtures.

Regarding thermal properties, Figure 12(b) presents the average thermal conductivity results from PAM test samples with different BFD contents. The reference sample exhibits a thermal conductivity of 1.53 W/m·K, while mixtures containing 2%, 4%, 6%, 8%, and 10% BFD show average values of 1.61, 1.64, 1.45, 1.53, and 1.51 W/m·K, respectively. Although M2 and M4 samples exhibited a slight increase in average thermal conductivity, an ANOVA at the 0.05 significance level showed no significant difference. This behaviour is consistent with theoretical models, which indicate that thermal conductivity in asphalt mixtures is primarily governed by the composition and distribution of thermally conductive additives such as BFD, whereas small variations in air void content have only a marginal effect on heat transfer in porous media [41]. The increases observed in M2 and M4 are attributed to the high conductivity of BFD and its interaction with the aggregate–binder matrix, rather than to the slight (1.6%) change in AVC from M0 to M10.

Accordingly, the low variation in results can be attributed to the thermal contributions of each constituent material and their distribution within the mixture; see CT scans in Figure 8(a). The high Fe-based compound content in BFD (75.6%, see Table 1) suggested that an enhancement of both thermal and electrical properties of the PAM could be anticipated. The expected thermal conductivity of the aggregates (mylonite) is 4.38 W/m·K, influenced by minerals such as quartz (7.70 W/m·K) and orthoclase (2.32 W/m·K) [42]. BFD, with higher oxide content, has an estimated conductivity of 7.07 W/m·K due to minerals including Fe_3O_4, Fe_2O_3, and FeO (see XRD results in Table 3), which have conductivities of 5.2, 12, and 10 W/m·K, respectively [43]. These values indicate that the thermal conductivity of mixtures is primarily governed by the binder, with a polymer-modified bitumen value of 0.19 W/m·K [44].

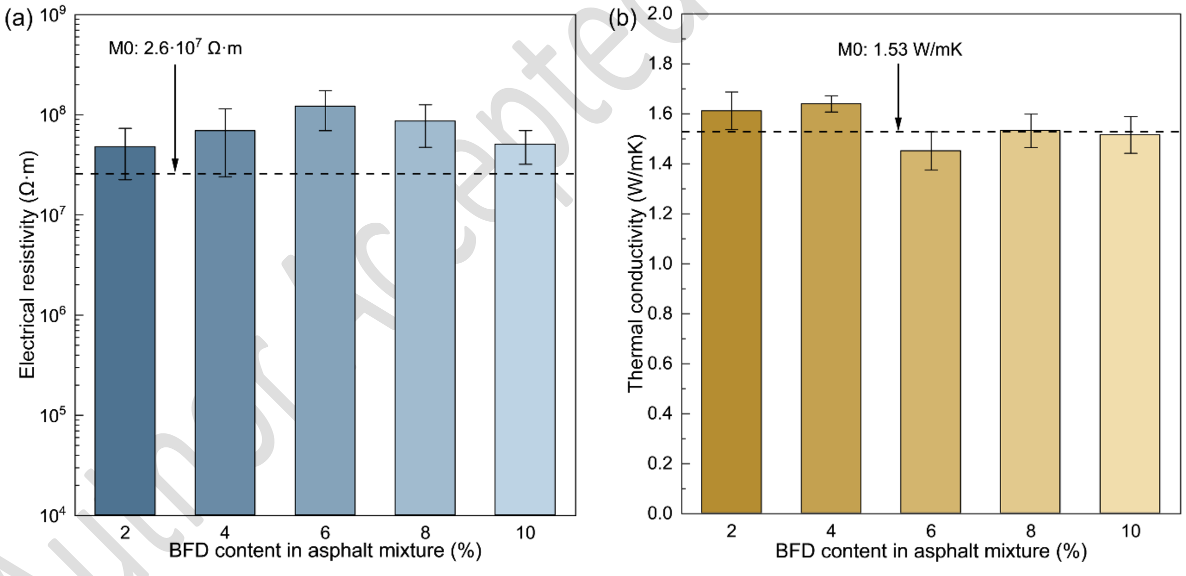

Figure 12. Average results of (a) electrical and (b) thermal properties of the mixtures with different BFD content.

This suggests that at high BFD content, metallic particles lead to clustering and uneven material distribution, resulting in a more dispersed structure with smaller voids, as shown in Figure 8. This behaviour is consistent with previous studies on metallic additives, where high dosages reduce thermal conductivity due to uneven material distribution [45]. In short, adding BFD has a minor effect on the thermal conductivity of porous asphalt, as the bitumen coating on BFD primarily influences the distribution and size of voids. A 4% BFD addition appears optimal for enhancing heat transfer, whereas higher contents may reduce thermal conductivity, potentially due to changes in internal structure or interactions with voids within the mixture.

3.4. Contribution of individual materials to the heating performance of PAM

Figure 13(a) shows the average surface temperature of the materials over microwave heating time, while thermographic images in Figure 13(b) and (c) depict the temperature distribution of fine aggregates and BFD, respectively, after 50 seconds of heating. Overall, an increase in temperature is observed over time for all the PAM samples, following a linear trend as characterised by their respective linear regression equations. To better understand the temperature, increase over time, a heating rate can be determined by the slope of the linear regression curves in Figure 13(a). BFD exhibited the highest heating rate at 0.88 °C/s, reaching an average temperature of 147 °C after 100 seconds. In contrast, bitumen showed the lowest temperature gradient of 0.14 °C/s, attaining 31 °C after the same heating period.

Among the studied aggregates, fine material exhibited the highest heating rate, followed by filler and coarse aggregates, with gradients of 0.41 °C/s, 0.33 °C/s, and 0.21 °C/s, respectively. As shown in Figure 13 (b), coarse, fine, and filler aggregates exhibited heterogeneous heating at high temperatures, whereas Figure 13 (c) shows that bitumen and BFD displayed homogeneous temperature distributions.

The observed differences in heating rates can be attributed to several factors: (i) material susceptibility to microwave heating, (ii) chemical composition, (iii) penetration depth and dielectric properties, (iv) moisture content, and (v) geometry [46, 47]. Materials differ in microwave susceptibility, transmitting, reflecting, or absorbing radiation to varying degrees, which affects volumetric heating. In PAM samples, metals are highly reflective, water strongly absorbs, and quartz is largely transparent [48], whereas bitumen is mostly inert, absorbing little heat and heating more slowly than other components. In terms of chemical composition, the particularly high susceptibility of BFD to microwave radiation heating is attributed to its high Fe content (75.6%), as shown in Table 1, which amplifies electromagnetic wave reflection and enhances material heating. Regarding the mineral aggregates (Mylonite), the high presence of quartz (34%) and feldspar (49%), as shown in Table 2, results in low susceptibility to heating [15], while the increased concentration of metals intensifies localised heating.

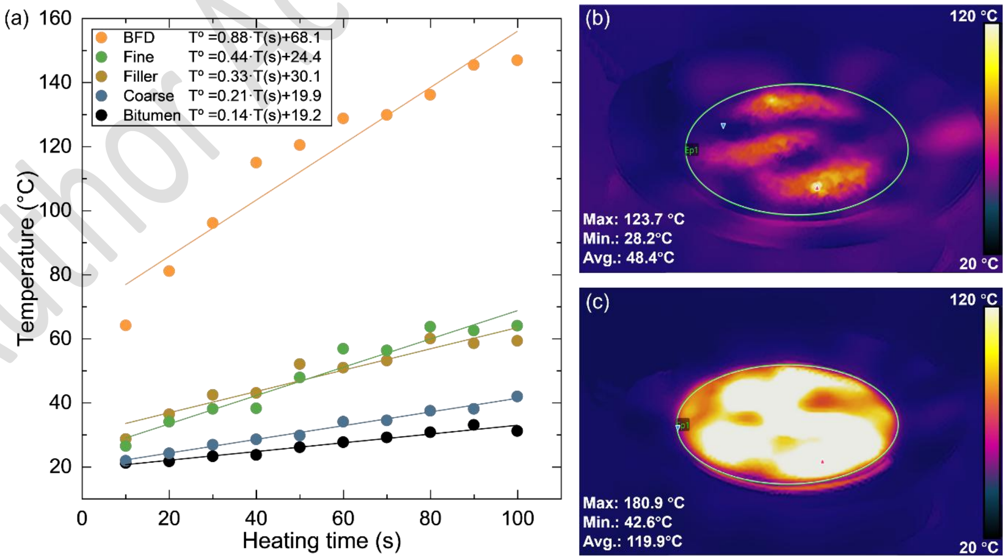

Figure 13. (a) Results of surface temperature versus heating time in the components of the porous asphalt mixture. Infrared images of the surface temperature of the (b) fine aggregate and (c) BFD at a heating time of 50 s.

The penetration depth of microwave radiation in mylonite-based aggregates is estimated to be 1.5 cm at 25°C [48]. For fine aggregates (4.75–0.08 mm) and mineral filler (<0.08 mm), penetration depth exceeds particle size, enabling most microwave absorption. Low water absorption in coarse and fine aggregates (Tables S2 and S3) limits moisture effects. Morphologically, sub-rounded to sub-angular coarse aggregates heat efficiently, while finer, spherical particles are more susceptible to microwave radiation.

With all these results in mind, it can be concluded that the steeper temperature gradient in fine aggregates and filler is primarily influenced by their geometry, particle distribution, and volume in the sample, which allows microwave absorption due to penetration depth. This makes them more susceptible to being heated compared to the coarse aggregate. The previous characterisation of the raw material composing PAM samples will provide valuable insights into how the composite bituminous material absorbs microwave radiation and distributes heat, impacting the mixture's performance.

3.5. Influence of BFD content on the microwave heating performance of PAM

The average surface temperature of PAM samples is shown as a function of heating time under microwave radiation (see Figure 14(a)). Overall, all mixtures exhibit a linear temperature increase over time, with heating rates rising from 0.52°C/s for M0 to 1.12 °C/s for M10 due to the susceptibility of PAM components to microwave heating (BFD > fine aggregate > filler > coarse aggregate > bitumen). Notably, between 10–40 s, M10 reaches a lower surface temperature than M8. From 50 s onwards, M10 matches M8 and surpasses it at 60 s, attaining 84.2 °C, with an average of 86.4 °C. The initially lower temperatures in M10 can be attributed to BFD distribution, where high dosages form clusters that act as isolated hot spots, reducing heat transfer.

Besides, Figure 14(b) presents the average energy consumption for each PAM sample and the optimal heating times, defined as the time required for the bitumen to reach its softening point (60 °C) based on the temperature curves in Figure 14(a). The softening point criterion was selected, as it is widely reported [10, 49, 50] as the optimal temperature for asphalt self-healing. Overall, it is seen that both variables decreased in value with the addition of BFD in the PAM samples, following a similar trend.

Energy consumption dropped from 105.5 Wh/kg (M0) to 50.5 Wh/kg (M10), showing that BFD addition increases energy efficiency, reducing consumption by up to 50%. Comparable results were observed in dense asphalt [23], where 9 wt.% fine slag replacement doubled energy efficiency. Heating time decreases from 75 s (M0) to 35 s (M10). Similar energy consumption and optimal heating times for M2–M4 and M8–M10 suggest comparable volumetric heating, consistent with their thermal properties (see Sections 3.1 and 3.3) and similar heating rates (Figure 14(a)).

As examples of heating at optimal times, Figure 14(c) and (d) show representative thermographic images of M0 and M4 samples heated during 75 s and 55 s, respectively, with their corresponding surface temperature distribution histograms shown in Figure 14(e) and (f). For M0, 30% of the surface was 50–70 °C and 33% above 70 °C, due to hot spots, porosity, and localised metals. Similar effects occur in M8 and M10. M4 showed a more uniform distribution, with 60% at 50–70 °C and 25% above 70 °C, like M2 and M6—greater bitumen exposure near the softening point permits controlled flow and healing.

Conversely, mixtures with larger surface areas exposed to temperatures above 70 °C may overheat, causing aggregate movement within the porous structure or loss due to excessive bitumen softening. This can reduce the mixture's ability to effectively close cracks over successive heating cycles. Similar observations were reported by Norambuena-Contreras and García [51] for dense asphalt mixtures with high metallic fibre content under microwave heating.

Overall, this analysis suggests that BFD contents up to 6% provide optimal thermal performance in PAM, avoiding excessive heating while promoting crack healing under consecutive microwave cycles, as will be evaluated in the following section.

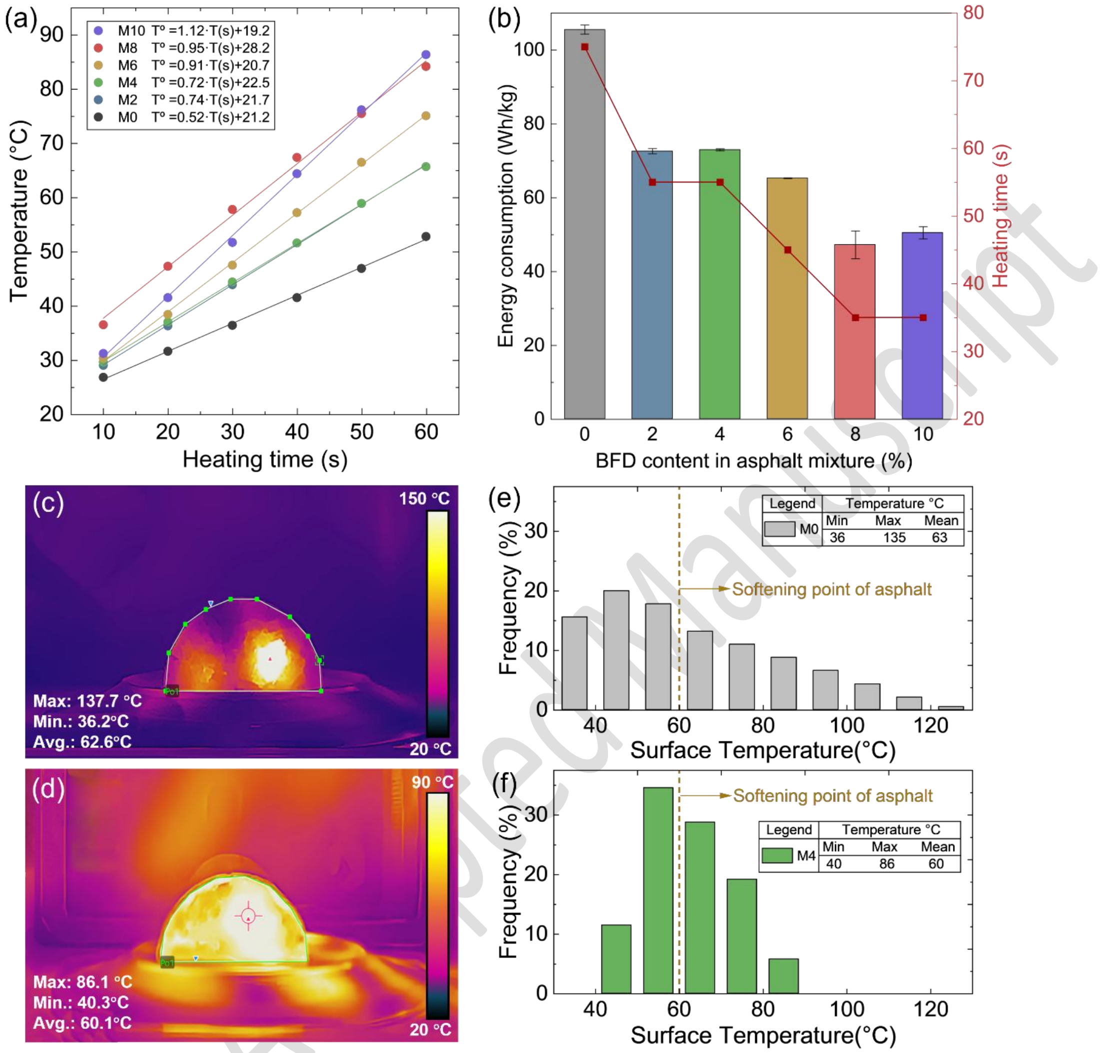

Figure 14. (a) Surface temperature over heating time for porous asphalt mixtures with and without BFD. (b) Energy consumption and optimal heating time for mixtures with different BFD contents. Infrared images of (c) M0 at 75 s and (d) M4 at 55 s. Histograms of surface temperature at the optimal heating time for (e) M0 at 75 s and (f) M4 at 55 s.

3.6. Influence of BFD content on the crack-healing performance of PAM

Average healing indices (HI) for PAM samples with different BFD contents across five crack-healing cycles are presented in Figure 15a. Overall, HI values ranged from 50% to 87%. The addition of BFD generally led to a decrease in HI compared with the M0 sample, although no clear trend was observed among BFD-containing mixtures. Regarding the effect of successive healing cycles, no distinct pattern was apparent, though a slight initial reduction in HI was noted. To better quantify the influence of both BFD content and healing cycles, a healing index improvement ratio was defined as follows in Eq. 1:

$$HI_i = \left(\frac{HI_{Ci} - HI_{C1}}{HI_{C1}}\right) x100 \tag{1}$$

where, HI_{Ci} is the healing index for cycles 2, 3, 4, and 5, and HI_{C1} is the healing index for cycle 1 for each BFD content. Since HI_i is a comparison against the first healing cycle, this variable can be interpreted as a performance parameter of the healing property under successive cycles. With this in mind, HI_i values tending to positive values indicate an improvement of the HI with the successive cycles, HI_i values close to zero indicate a trend of maintaining the HI with the successive cycles, and HI_i tending to negative values, meaning a decay in the HI with the successive cycles.

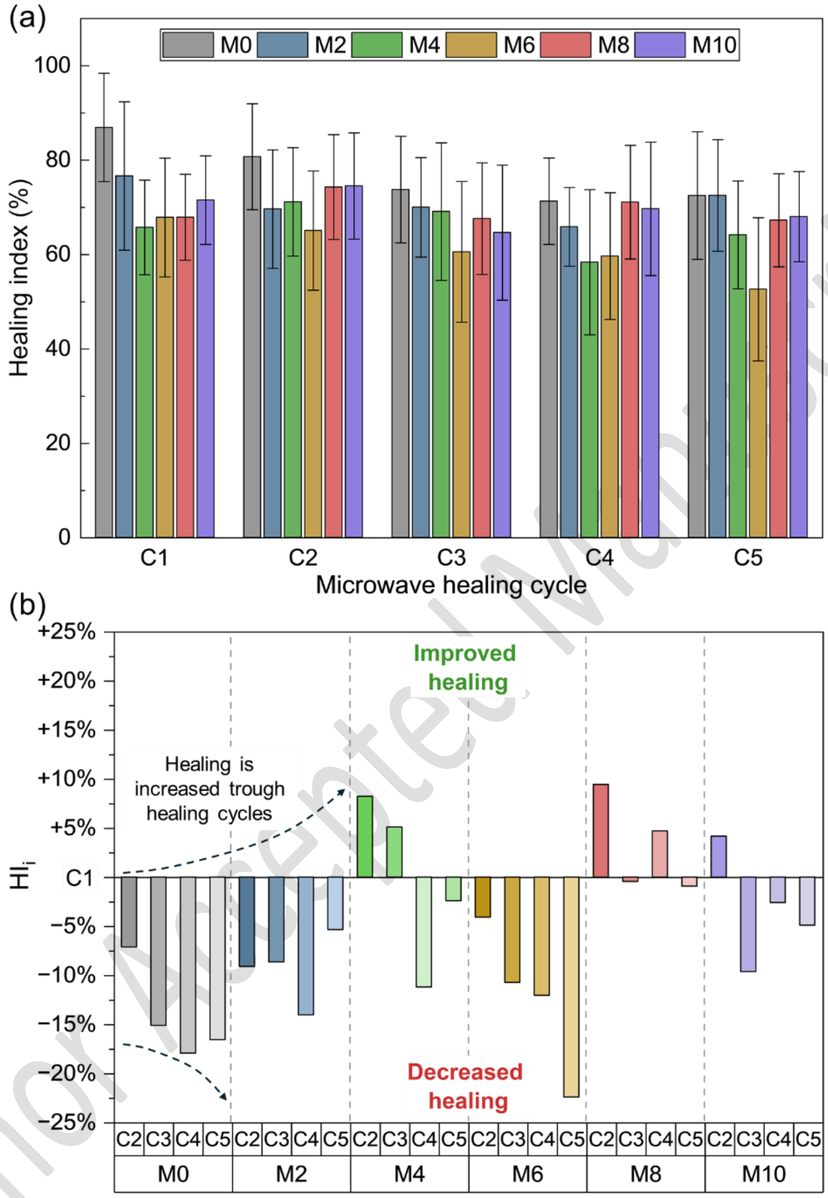

Figure 15. (a) Average healing index results for asphalt mixtures M0–M10 across healing cycles C1–C5, and (b) results of healing index improvement (HI_i) for asphalt mixtures M0–M10 and healing cycles C2–C5.

On the other hand, Figure 15b shows an overall reduction of the HI_i values with the healing cycles, regardless of the BFD content. For M0 and M2, the consecutive healing cycles notably decreased the HI compared to the initial healing C1. The observed decay in HI_i over successive healing cycles can be attributed to insufficient heating in the crack zone, which reduced the crack-closure efficiency of the initially damaged sample.

Consequently, the similar trend identified for both M0 and M2 meant that 2% BFD was not enough to maintain the healing performance through successive cycles. When the BFD content increased to 4%, Figure 15b reveals an increase in the HI_i for the healing cycles C2 and C3, with variations of +8% and +5% with respect to C1, respectively. These results suggest that during healing cycles C1–C3, M4 experienced more uniform heating across the crack zone, effectively promoting closure. This is supported by the previous infrared temperature distribution analysis, which showed 60% of the surface between 50 °C and 70 °C, allowing the mixture to maintain its structure and mechanical integrity throughout the cycles. A decay in HI_i is then observed for cycles C4 and C5.

In the same way, samples M6, M8, and M10 presented high negative HI_i. These results can be explained by a local overheating of the BFD in the sample, promoting the bitumen to flow into voids near the failure zone together with a change in the aggregates position, reducing the strength of the PAM sample in the cracked area. Based on the previous analysis of the HI_i, it can be concluded that the addition of 4% BFD promotes a consistent healing for up to three successive healing cycles in a PAM.

To evaluate if the variations in the HI previously analysed are statistically significant, Table 4 summarises the ANOVA results, evaluating the individual and combined effect of the BFD and healing cycle. Regarding the individual effect of the BFD content, the average HI values were ordered as M0 (77.1%) > M2 (70.9%) > M10 (69.7%) > M8 (69.6%) > M4 (65.7%) > M6 (61.2%). The least significant difference (LSD) pairwise mean comparisons (see Table 4) showed significant differences between M0 and the samples with BFD contents. Among the samples with BFD, significant differences were identified between samples M6 and M2, M8, and M10. Consequently, it can be concluded that the addition of BFD has a significant effect on reducing the HI values compared with M0. Additionally, among the samples incorporating BFD, differences between M2 (the sample with the highest HI value) and M4 (the sample presenting uniform heating) were not significant, validating the previous selection of 4% BFD as an appropriate content to be selected for healing purposes.

Regarding the individual effect of the healing cycle, the average HI values were ordered as C1 (72.7%) > C2 (72.6%) > C3 (67.1%) > C5 (66.2%) > C4 (66.0%). For this study variable, the LSD pairwise mean comparisons (see Table 4) showed significant differences except between C1 – C2, C3 – C4 (C5), and C4 – C5. These results suggest that during the first two consecutive cycles, the healing performance of the samples tends to be similar, with consistently high HI values. However, starting from the third healing cycle, the similarly low HI suggests that the samples were affected by a possible overheating effect as previously explained, reducing the healing performance of the PAM samples.

Table 4. ANOVA *p-values* and LSD post-hoc test evaluating the statistical effect of the BFD content and healing cycle on the healing index (HI).

Variable	***HI p-value***	**LSD - Significant differences**
X	<0.001	M0 – M2 (M4; M6; M8; M10) M6 – M2 (M8; M10)
Y	0.0059	C1 – C3 (C4; C5) C2 – C3 (C4; C5)
X*Y	0.7341	No significant differences

Note: X: BFD content (M0, M2, M4, M6, M8, M10); Y: Healing cycle (C1, C2, C3, C4, C5).

As a result, the healing process should be limited to no more than two successive cycles to avoid significantly reducing the healing performance of PAM samples. Nonetheless, given the particularly positive HI_i value obtained for the M4 in the third healing cycle, this sample could withstand an additional consecutive healing cycle compared with the rest of the samples. Finally, no statistically significant interaction between BFD content and the healing cycle was found, as shown in Table 4.

In summary, the analysis indicates that healing performance is influenced by both BFD addition and AVC reduction in the mixtures. For effective on-site maintenance, heating porous asphalt mixtures with 4% BFD for approximately 55 s is recommended, ensuring consistent crack-healing across cycles. The uniform heating provided by BFD supports prolonged healing under microwave radiation, maintaining stable mechanical performance with each cycle and demonstrating the potential for constructing durable roads with enhanced crack-healing capabilities.

3.7. Summary and scoring for measured variables

Table 5 summarises the effect of BFD addition on the properties of PAM, expressed as percentage variations relative to M0. Results were scored as increase, decrease, or steady, with steady representing no effect on the measured variable. Physical and hydraulic results indicate that higher BFD contents progressively reduce air-void content and permeability, especially in mixtures M6–M10, as excessive fine replacement constricts the void network and impairs hydraulic efficiency. In contrast, moderate replacement (see M4) maintains both permeability and a stable void structure, which is critical for SUDS applications. From a mechanical perspective, BFD clearly enhances resistance to particle loss and increases the stiffness modulus, especially under wet conditions, indicating improved aggregate–binder interaction and overall structural integrity. However, excessive BFD contents (M8–M10) increase moisture sensitivity and reduce strength ratio stability, highlighting a trade-off between mixture densification and moisture susceptibility. Regarding electro-thermal properties, variations in electrical resistivity do not significantly affect electromagnetic behaviour, while thermal conductivity exhibits only marginal changes, particularly for M4.

Conversely, microwave heating influences the measured properties. The efficiency of microwave heating rises significantly with BFD content, reflecting the strong microwave responsiveness of steel-industry residues. Nevertheless, the healing index declines as BFD content increases, owing to reduced air-void content and limited binder mobility, indicating that heating efficiency alone is insufficient to achieve optimal healing. Table 5 shows that BFD incorporation results in multivariable effects in PAM, and that moderate replacement levels (M4) provide the best overall performance. This emphasises the need to optimise BFD content rather than simply maximise microwave susceptibility when designing SUDS-compatible, self-healing pavements.

Table 5. Multivariable comparison of PAM containing BFD (M2-M10) with respect to M0 (values in %).

Property Type	**Measured Variable**	**Porous Asphalt Mixtures (PAM) with BFD**				
		M2	**M4**	**M6**	**M8**	**M10**
Physical	Bulk density	🟧 (0.4)	🟧 (0.4)	🟧 (-0.1)	🟧 (0.3)	🟧 (-0.3)
	Air Void Content	🟧 (-3)	🟧 (-5)	▼(-6)	▼(-7)	▼(-8)
Hydraulic	Permeability	🟧 (-15)	🟧 (-2)	▼(-12)	▼(-28)	▼(-27)
Mechanical	Particle loss (Dry)	▲(20)	▲(15)	▲(12)	▲(9)	▲(55)
	Particle loss (Wet)	🟧 (1)	▲(38)	▲(15)	▲(36)	▲(12)
	Strength Ratio	🟧 (-2)	🟧 (-4)	▼(-9)	🟧 (2)	🟧 (-3)
	Stiffness modulus at 25°C	🟧 (0)	▲(17)	▲(9)	▲(14)	▲(92)
Electro-thermal	Electrical resistivity	🟧 (4)	🟧 (6)	🟧 (9)	🟧 (7)	🟧 (4)
	Thermal conductivity	🟧 (5)	▲(7)	▼(-5)	🟧 (0)	🟧 (1)
Microwave heating	Heating efficiency	▲(42)	▲(38)	▲(75)	▲(83)	▲(115)
	Healing index	▼(-8)	▼(-15)	▼(-21)	▼(-10)	▼(-10)

Scoring notation: ▲ Increase ▼ Decrease 🟧 Steady

4. Conclusions

This study evaluated the effect of replacing fine aggregate with BFD on the physical, hydraulic, mechanical, electrical, thermal, and microwave crack-healing properties of porous asphalt mixtures, supported by a detailed physical and chemical characterisation of the materials. From the analysis of the results, the following main conclusions can be drawn:

- The addition of BFD to porous asphalt reduced the air void content by lowering the maximum density, owing to the internal porosity of BFD, as revealed by µCT reconstruction analysis. A 4% BFD addition maintained well-distributed voids, ensuring efficient water flow, while higher BFD levels created smaller voids, reducing permeability by up to 27% compared to the reference mixture without BFD addition.
- Mixtures with 4% BFD (M4) showed superior mechanical performance compared with the reference mixture (M0), with greater resistance to particle loss, higher indirect tensile strength in both dry and wet conditions, and an increased stiffness modulus, largely due to reduced AVC. The iron oxides in BFD enhanced bitumen adhesion, while its angularity, porosity, and distribution improved mortar cohesion.
- The addition of BFD did not significantly affect electrical resistivity or thermal conductivity, owing to the shielding effect of bitumen and the dispersion of the metallic additive. All porous mixtures remained in the insulating phase, while 4% BFD (M4) optimised heat transfer.
- Microwave exposure showed the highest heating rate for BFD, followed by fine aggregate, filler, coarse aggregate, and bitumen. Increasing BFD content in PAM enhanced the heating rate, reducing both energy demand and the optimal healing time for bitumen fluidity. An 8% addition (M8) doubled the efficiency of the reference mixture (M0).
- All porous asphalt mixtures, with or without BFD, exhibited comparable healing indices, ranging from 60 to 80%. The bitumen heating time, based on the softening point, was found to be optimal for effective self-healing in PAM.
- Statistical analysis showed a general decline in healing indices for PAM–BFD mixtures from the third successive healing cycle. Among them, M4 achieved a healing index comparable to the best-performing sample and sustained an additional third cycle without adverse effects.
- This study concluded that PAM with 4% BFD is recommended for crack-healing via external microwave heating, as it maintains structural integrity and hydraulic performance through uniform heat distribution and controlled bitumen flow, thereby promoting multifunctional asphalt for self-healing permeable roads.

Funding: This research was partially funded by the Universidad Pedagógica y Tecnológica de Colombia under project reference SGI 3472. X-ray microCT facilities were provided by the Swansea University Advanced Imaging of Materials (AIM) Core Facility; funded in part by the EPSRC (EP/M028267/1) and the European Regional Development Fund through the Welsh Government (80708).

Acknowledgements: The authors would like to acknowledge the technical support of Kimena Rojo from LabMAT-Chile and Jose Manuel Sierra from the Pavement Laboratory at the Universidad Pedagógica y Tecnológica de Colombia.

Conflicts of Interest: The authors declare that they have no known competing financial interests or personal relationships that could have influenced the work reported in this paper.

Supplementary Information: Figure S1. Detailed composition of the materials used in manufacturing porous asphalt mixtures. **Figure S2:** Phase composition diagram of porous asphalt mixtures; **Table S1.** Physical and mechanical properties of bitumen PG 76-22; **Table S2.** Physical and mechanical properties of coarse aggregate, and **Table S3.** Physical properties of fine aggregates. **Video S1.** 3D µCT reconstruction of M4.

Data available on request from the authors: The data that support the findings of this study are available from the corresponding author, [J.N-C], upon reasonable request.

5. References

1. United Nations (2023) The Sustainable Development Goals Report 2023. The Sustainable development Goals Report 2023: Special Edition 80

2. Senior-Arrieta V, Graciano C (2020) A review of design, construction, and performance of permeable asphalt mixes in rainy countries: case of Colombia. International Journal of Pavement Research and Technology. https://doi.org/10.1007/s42947-020-0023-2

3. Watson D, Tran NH, Rodezno C, et al (2018) Performance-Based Mix Design for Porous Friction Courses. NCHRP 877. National Academies Press. TRB. Washington.

4. Woods-Ballard B, Wilson S, Udale-Clarke H, et al (2015) The SuDS Manual. Ciria. London.

5. Garcia A, Aboufoul M, Asamoah F, Jing D (2019) Study the influence of the air void topology on porous asphalt clogging. Constr Build Mater 227:116791. https://doi.org/10.1016/j.conbuildmat.2019.116791

6. Norambuena-Contreras J, Serpell R, Valdés Vidal G, et al (2016) Effect of fibres addition on the physical and mechanical properties of asphalt mixtures with crack-healing purposes by microwave radiation. Constr Build Mater 127:369–382. https://doi.org/10.1016/j.conbuildmat.2016.10.005

7. Liang B, Lan F, Shi K, et al (2020) Review on the self-healing of asphalt materials: Mechanism, affecting factors, assessments and improvements. Constr Build Mater 266:120453. https://doi.org/10.1016/j.conbuildmat.2020.120453

8. Sarsam SI (2015) Crack Healing Potential of Asphalt Concrete Pavement. International Journal of Scientific Research in Knowledge 3:1–12. https://doi.org/10.12983/ijsrk-2015-p0001-0012

9. García Á (2012) Self-healing of open cracks in asphalt mastic. Fuel 93:264–272. https://doi.org/10.1016/j.fuel.2011.09.009

10. Liu Q (2012) Induction Healing of Porous Asphalt Concrete. Dissertation, Delft University of Technology

11. Tabaković A, O'Prey D, McKenna D, Woodward D (2019) Microwave self-healing technology as airfield porous asphalt friction course repair and maintenance system. Case Studies in Construction Materials 10:. https://doi.org/10.1016/j.cscm.2019.e00233

12. Xu S, Liu X, Tabaković A, Schlangen E (2021) The prospect of microwave heating: Towards a faster and deeper crack healing in asphalt pavement. Processes 9:. https://doi.org/10.3390/pr9030507

13. Zhu X, Ye F, Cai Y, et al (2019) Self-healing properties of ferrite-filled open-graded friction course (OGFC) asphalt mixture after moisture damage. J Clean Prod 232:518–530. https://doi.org/10.1016/j.jclepro.2019.05.353

14. Norambuena-contreras J, Gonzalez-torre I (2017) Influence of the Microwave Heating Time on the Self-Healing Properties of Asphalt Mixtures. https://doi.org/10.3390/app7101076

15. Trigos L, Gallego J, Escavy JI (2020) Heating potential of aggregates in asphalt mixtures exposed to microwaves radiation. Constr Build Mater 230:117035. https://doi.org/10.1016/j.conbuildmat.2019.117035

16. Zhang F, Cao Y, Sha A, et al (2022) Characterization of asphalt mixture using X-ray computed tomography scan technique after freeze-thaw cycle and microwave heating. Constr Build Mater 346:128435. https://doi.org/10.1016/j.conbuildmat.2022.128435

17. Atakan M, Yildiz K (2022) Self-Healing Potential of Porous Asphalt Concrete Containing Different Aggregates and Metal Wastes Through Microwave Heating. Politeknik Dergisi 25:623–631. https://doi.org/10.2339/politeknik.810673

18. Ochoa-díaz R (2021) Use of blast furnace dust to improve the properties of granular material for pavements Uso de polvo de alto horno para mejorar las propiedades de material granular para pavimentos. 20:135–143. https://doi.org/10.18273/revuin.v20n4-2021011.136

19. Das B, Prakash S, Reddy PSR, Misra VN (2007) An overview of utilization of slag and sludge from steel industries. Resour Conserv Recycl 50:40–57. https://doi.org/https://doi.org/10.1016/j.resconrec.2006.05.008

20. Phan TM, Park DW, Le THM (2018) Crack healing performance of hot mix asphalt containing steel slag by microwaves heating. Constr Build Mater 180:503–511. https://doi.org/10.1016/j.conbuildmat.2018.05.278

21. Gao J, Sha A, Wang Z, et al (2017) Utilization of steel slag as aggregate in asphalt mixtures for microwave deicing. J Clean Prod 152:429–442. https://doi.org/10.1016/j.jclepro.2017.03.113

22. Wang H, Zhang Y, Zhang Y, et al (2019) Laboratory and numerical investigation of microwave heating properties of asphalt mixture. Materials 12:. https://doi.org/10.3390/ma12010146

23. Gulisano F, Crucho J, Gallego J, Picado-Santos L (2020) Microwave healing performance of asphalt mixture containing electric arc furnace (EAF) slag and graphene nanoplatelets (GNPs). Applied Sciences (Switzerland) 10:. https://doi.org/10.3390/app10041428

24. Lou B, Sha A, Barbieri DM, et al (2021) Characterization and microwave healing properties of different asphalt mixtures suffered freeze-thaw damage. J Clean Prod 320:128823. https://doi.org/10.1016/j.jclepro.2021.128823

25. ASTM D3203 (2022) Standard Test Method for Percent Air Voids in Compacted Asphalt Mixtures

26. FDOT (2014) FM 5-565. MEASUREMENT OF WATER PERMEABILITY OF COMPACTED ASPHALT PAVING MIXTURES. Gainesville, Florida

27. NLT-352/86 (1986) Caracterizacion de las mezclas bituminosas abiertas por medio del ensayo cantabro de perdida por desgaste. España, pp 5–6

28. Alvarez AE, Epps-Martin A, Estakhri C, Izzo R (2010) Evaluation of durability tests for permeable friction course mixtures. International Journal of Pavement Engineering 11:49–60. https://doi.org/10.1080/10298430902730539

29. ASTM 7064 (2013) Open-Graded Friction Course (OGFC) Mix Design. ASTM

30. AEN (2019) Bituminous Mixtures – Test Methods – Part 26: Stiffness. Spain, UNE-EN 12697-26

31. Norambuena-Contreras J, Gonzalez A, Concha JL, et al (2018) Effect of metallic waste addition on the electrical, thermophysical and microwave crack-healing properties of asphalt mixtures. Constr Build Mater 187:1039–1050. https://doi.org/10.1016/j.conbuildmat.2018.08.053

32. Norambuena-Contreras J, Concha JL, Varela MJ, et al (2024) Microwave Heating and Self-Healing Performance of Asphalt Mixtures Containing Metallic Fibres from Recycled Tyres. Materials 17:1–21. https://doi.org/10.3390/ma17235950

33. Norambuena-Contreras J, Asanza Izquierdo E, Castro-Fresno D, et al (2013) A new model on the hydraulic conductivity of asphalt mixtures. International Journal of Pavement Research and Technology 6:488–495. https://doi.org/10.6135/ijprt.org.tw/2013.6(5).488

34. Omar HA, Yusoff NIM, Mubaraki M, Ceylan H (2020) Effects of moisture damage on asphalt mixtures. Journal of Traffic and Transportation Engineering (English Edition) 7:600–628. https://doi.org/10.1016/j.jtte.2020.07.001

35. Masad E, Tashman L, Little D, Zbib H (2005) Viscoplastic modeling of asphalt mixes with the effects of anisotropy, damage and aggregate characteristics. Mechanics of Materials 37:1242–1256. https://doi.org/10.1016/j.mechmat.2005.06.003

36. López-Contreras YF, (2017) Effect of physicochemical heterogeneity on adhesion phenomenon between bitumen and aggregates in asphalt mixtures. Dissertation, Universidad Industrial de Santander.

37. Sun G, Niu Z, Zhang J, et al (2022) Impacts of asphalt and mineral types on interfacial behaviors: A molecular dynamics study. Case Studies in Construction Materials 17:e01581. https://doi.org/10.1016/j.cscm.2022.e01581

38. Hesami S, Ameri M, Goli H, Akbari A (2015) Laboratory investigation of moisture susceptibility of warm-mix asphalt mixtures containing steel slag aggregates. International Journal of Pavement Engineering 16:745–759. https://doi.org/10.1080/10298436.2014.953502

39. Ochoa-díaz R (2019) Estudio Del Comportamiento De Concreto Asfáltico Con Residuos Siderúrgicos Como Agregados. Dissertation, Universidad Pedagógica Y Tecnológica De Colombia

40. Gulisano F, Jimenez-Bermejo D, Castano-Solís S, et al (2024) Development of Self-Sensing Asphalt Pavements: Review and Perspectives. Sensors 24:. https://doi.org/10.3390/s24030792

41. Chen J, Wang H, Li L (2015) Determination of Effective Thermal Conductivity of Asphalt Concrete with Random Aggregate Microstructure. Journal of Materials in Civil Engineering 27:. https://doi.org/10.1061/(asce)mt.1943-5533.0001313

42. Somerton WHBT-D in PS (1992) Chapter V. Thermal Conductivity of Rock/Fluid Systems. In: Thermal properties and temperature-related behavior of rock/fluid systems. Elsevier, pp 39–8. Amsterdam

43. Takeda M, Onishi T, Nakakubo S, Fujimoto S (2009) Physical properties of iron-oxide scales on Si-containing steels at high temperature. Mater Trans 50:2242–2246. https://doi.org/10.2320/matertrans.M2009097

44. Pan P, Wu S, Hu X, et al (2017) Effect of material composition and environmental condition on thermal characteristics of conductive asphalt concrete. Materials 10:. https://doi.org/10.3390/ma10030218

45. Yinfei D, Jiacheng W, Jiaqi C (2021) Cooling asphalt pavement by increasing thermal conductivity of steel fiber asphalt mixture. Solar Energy 217:308–316. https://doi.org/10.1016/j.solener.2021.02.030

46. Mishra RR, Sharma AK (2016) Microwave-material interaction phenomena: Heating mechanisms, challenges and opportunities in material processing. Compos Part A Appl Sci Manuf 81:78–97. https://doi.org/10.1016/j.compositesa.2015.10.035

47. Hu Q, He Y, Wang F, et al (2021) Microwave technology: a novel approach to the transformation of natural metabolites. Chinese Medicine (United Kingdom) 16:1–22. https://doi.org/10.1186/s13020-021-00500-8

48. Mello PA, Barin JS, Guarnieri RA (2014) Microwave Heating. In: Microwave-Assisted Sample Preparation for Trace Element Analysis. Elsevier, Brazil, pp 59-75

49. Tang J, Liu Q, Wu S, et al (2016) Investigation of the optimal self-healing temperatures and healing time of asphalt binders. Constr Build Mater 113:1029–1033. https://doi.org/10.1016/j.conbuildmat.2016.03.145

50. Xu S (2020) Self-healing Porous Asphalt: A Combination of Encapsulated Rejuvenator and Induction Heating. Dissertation, Delft University of Technology

51. Norambuena-Contreras J, Garcia A (2016) Self-healing of asphalt mixture by microwave and induction heating. Mater Des 106:404–414. https://doi.org/10.1016/j.matdes.2016.05.095